24
Atomistic-Level Models

Jennifer Wilcox

24.1
Introduction

Understanding the speciation of mercury throughout the coal-combustion process is crucial to the design of efficient and effective mercury removal technologies. Mercury oxidation takes place through combined homogeneous (i.e., strictly in the gas phase) and heterogeneous (i.e., gas–surface interactions) pathways. Both bench-scale combustion experiments [1] and quantum-chemistry-based theoretical model efforts [2, 3] indicate that homogeneous mercury oxidation is responsible for, at most, 10% of the overall oxidation in a typical coal-fired flue gas with chlorine levels at 500 ppmv (e.g., HCl equivalent). These studies have been additionally confirmed by recent work that compares model predictions to bench-scale experiments, with the simulation predictions dependent on previous kinetic submodels developed specifically for Hg oxidation [4, 5]. Mercury speciation in coal-fired flue gases are extremely complex and depend on many factors, some of which include the mineralogy and chemistry of the coal, combustion conditions, power plant configuration, flue-gas composition, and temperature-time history from the boiler to the stack.

The extent to which particulate-bound mercury (Hg_p), gaseous oxidized mercury (Hg^{2+}), and gaseous elemental mercury (Hg^0) are emitted from the stack is also dependent on the existing pollution controls in a given power plant. The effective removal of Hg through existing flue-gas control technologies acts as a co-benefit (as discussed elsewhere in this book). For instance, electrostatic precipitators (ESPs), in particular cold-side ESPs and hot-side ESPs, capture, on average, 27% and 4% of Hg, while fabric filters (FFs) are more effective with approximately 58% Hg removal [6]. In general, Hg_p or Hg^{2+} is easier to capture using one of these control technologies. In addition, oxidized Hg may also be captured in existing flue-gas desulfurization (FGD) units as the oxidized form is water-soluble. Activated carbon injection (ACI) is a direct method used for Hg capture, in which powdered activated carbon (PAC) is injected into the plant's flue-gas stream where it adsorbs gaseous Hg and is collected in downstream particulate control devices, such as FFs or ESPs. Heterogeneous investigations include both adsorption and

Mercury Control: for Coal-Derived Gas Streams, First Edition.
Edited by Evan J. Granite, Henry W. Pennline and Constance Senior.

oxidation mechanisms associated with natural surfaces present in the flue gas such as fly ash, but also include surfaces associated with existing control technologies, such as selective catalytic reduction (SCR) catalysts or specific Hg-control technologies such as activated carbon (AC) or precious-metal sorbents and catalysts. The fundamental model investigations carried out to date may be classified into three major categories: homogeneous Hg oxidation kinetics, chemisorption on AC, and adsorption and amalgamation of Hg with precious metals.

24.2 Homogeneous Mercury Oxidation Kinetics

24.2.1 Mercury–Chlorine Chemistry

Gas-phase oxidation occurs primarily via chlorine species originally present in the coal as the gases cool down through the air preheater and air pollution control devices. Thermodynamic calculations predict that Hg oxidation occurs at temperatures below approximately 700 °C and that Hg will be completely oxidized at or below 450 °C [7]. Regardless of the thermodynamic equilibrium model predictions, experimental evidence has found that not all of the Hg is oxidized in the flue gas, regardless of the chlorine content of the coal. These experimental findings have led the Hg control community to determine that Hg oxidation is kinetically, rather than thermodynamically, limited [7]. For this reason, there has been significant investigation of determining accurate Hg oxidation kinetics from quantum-mechanical-based estimates because of the difficulty of the flue-gas measurements.

Some of the first studies to include quantum chemistry into the examination of the oxidation kinetics of Hg for flue-gas applications are those of Sliger *et al*. [8, 9], in which a homogeneous kinetic model for Hg oxidation via chlorine was determined and coupled with bench-scale combustion experiments. On the basis of these experiments, it was found that oxidation increases with increasing HCl concentration, which is consistent with previous experiments carried out by Hall *et al*. [10, 11] Adding to these initial investigations, the work of Wilcox *et al*. [12–14] and Krishnakumar and Helble [15] provide a fairly complete set of Hg oxidation kinetics via Cl-containing compounds for the following set of reactions:

$$Hg + Cl \leftrightarrow HgCl \tag{R1}$$

$$Hg + O \leftrightarrow HgO \tag{R2}$$

$$Hg + Cl_2 \leftrightarrow HgCl + Cl \tag{R3}$$

$$Hg + Cl_2 \leftrightarrow HgCl_2 \tag{R4}$$

$$Hg + HCl \leftrightarrow HgCl + H \quad \text{(R5)}$$

$$Hg + HOCl \leftrightarrow HgCl + OH \quad \text{(R6)}$$

$$HgCl + Cl \leftrightarrow HgCl_2 \quad \text{(R7)}$$

$$HgCl + Cl_2 \leftrightarrow HgCl_2 + Cl \quad \text{(R8)}$$

$$HgCl + HCl \leftrightarrow HgCl_2 + H \quad \text{(R9)}$$

$$HgCl + HOCl \leftrightarrow HgCl_2 + OH \quad \text{(R10)}$$

Reactions 1, 2, 4, and 7 are all unimolecular decomposition reactions in the reverse direction and are often writing in terms of a collision partner "M" on either side of the reaction. The collision partner is omitted here and as such the rate constants reported herein are in units of $cm^3\,mol\,s^{-1}$ for the forward directions and s^{-1} for the reverse directions. If the concentration of the collision partner is taken into account, the forward direction of the recombination reactions would have units of $cm^6\,mol^2\,s^{-1}$. The remaining reactions are classified as bimolecular with reported units of $cm^3\,mol\,s^{-1}$. A variety of quantum-mechanical-based approaches have been carried out to accurately predict the rate constants of R1–R10. As there are limited experimental data available for these reactions, especially at high temperature, the levels of theory employed have been benchmarked against available experimental structural and thermochemical data. A comparison of predicted to measured vibrational frequency and bond distance data is presented in Tables 24.1 and 24.2, respectively. The levels of theory considered in Tables 24.1 and 24.2 are based on previous high-level kinetics predictions that have relied on these combined methods and basis set choices. The methods that have resulted in the most accurate predictions include B3LYP, MP2, MP4, QCISD, QCISD(T), and CCSD(T), and have been used alongside a variety of basis sets. Owing to the large number of electrons in Hg [16], basis sets incorporating relativistic effects for the inner-core electrons are required. The work of Wilcox *et al*. on Hg oxidation via Cl-containing compounds has relied primarily upon two basis sets, that is, the "60VDZ" basis set of the Stevens *et al*. [17] group and the "60MDF" basis set of the Stuttgart [18] group. Both of these basis sets replace 60 of Hg's atomic core electrons with a relativistic effective core potential. The work of Krishnakumar and Helble [15] has relied upon the "SDD" basis set for Hg, which uses Stuttgart [18] pseodopotentials, in addition to the "CEP-121G" basis set, which uses pseodopotentials developed from the Stevens [17] group. For the non-Hg species, either the D95++(3df,3pd) or the Pople 6-311++G(3pd,3df) basis set was used. Both of these basis sets include diffused and polarization functions on the O, Cl, Br, and H atoms. For the prediction of Hg oxidation via Br-containing compounds, Wilcox and Okano [19] used the augmented correlation-consistent basis set developed by Peterson *et al*. [20, 21], termed *AVTZ*.

Table 24.1 Comparison between experimental and theoretical vibrational frequencies (cm^{-1}) for various mercury-containing compounds.

Molecular species	Vibrational frequency (cm^{-1})		Level of theory[a)]
	Experiment	Prediction	
HgCl	292.61 [22];	244.4	B3LYP/60VDZ
	298.97 [23]	280.6	QCISD(T)/SDD
		285.5	MP4/SDD
		290.3	QCISD/CEP-121G
		290.6	QCISD/60VDZ
		303.0	MP2/CEP-121G
HgBr	188.3 [24]	153.8	CCSD(T)/AVTZ
		162.7	B3LYP/60MDF
HgO	NA	390	QCISD(T)/60VDZ
$HgCl_2$ (symmetric stretch)	313–366 [25, 26]	318	B3LYP/60VDZ
		340	QCISD/60VDZ
(Bend)	100 [27]	92	B3LYP/60VDZ
		97	QCISD/60VDZ
(Asymmetric stretch)	376–413 [28]	374	B3LYP/60VDZ
		394	QCISD/60VDZ
$HgBr_2$ (symmetric stretch)	218–229 [29–32]	201	B3LYP/60MDF
		218	CCSD(T)/AVTZ
(Bend)	68 [27]	60	B3LYP/60MDF
		67	CCSD(T)/AVTZ
(Asymmetric stretch)	293 [33]	271	B3LYP/60MDF
		289	CCSD(T)/AVTZ

a) All predictions from Wilcox *et al.* [12–14, 19] with the exception of SDD and CEP-121G basis sets, which were sourced from Krishnakumar and Helble [15].

The predicted vibrational frequencies of the ground states of HgCl, HgBr, HgO, $HgCl_2$, and $HgBr_2$, have all been compared to experimental data, except in the case of HgO, in which experimental data was unavailable. There have been two experimental reports of the single vibrational mode of HgCl reported in the literature, that is, 292.61 [22] and 298.97 cm^{-1} [23] and a number of experimental investigations [25–28] on the vibrational modes of $HgCl_2$. From Table 24.1 it can be seen that the QCISD (CEP-121G, 60VDZ) and MP2/CEP-121G levels of theory agree best with experiment. In addition, the QCISD/60VDZ level of theory was also able to accurately predict the vibrational frequencies of $HgCl_2$. A number of experimental measurements [24, 27, 29–31, 33] have also been made on HgBr and $HgBr_2$, and a comparison of experiment to prediction shown in Table 24.1 indicates that the CCSD(T)/AVTZ level of theory is the most accurate.

Table 24.1 also includes a comparison of the predicted equilibrium bond distances to available measured data. Experimental measurements [34–36] of HgCl bond distances range from 2.23 to 2.50 Å. All of the levels of theory investigated predict bond distances within this range. The experimental bond distances [34, 38, 39] for $HgCl_2$ range from 2.25 to 2.44, and again, both levels of theory considered

Table 24.2 Comparison between experimental and theoretical bond lengths (Å) for various mercury-containing compounds.

Molecular species	Bond length (Å)		Level of theory[a)]
	Experiment	Prediction	
HgCl	2.23–2.50 [34–36]	2.40	MP4/SDD
		2.41	QCISD (CEP-121G; 60VDZ) QCISD(T)/SDD
		2.48	B3LYP/60VDZ
		2.49	MP2/CEP-121G
HgBr	2.62 [24]	2.62	B3LYP/60VDZ
		2.64	B3LYP/60MDF
		2.70	CCSD(T)/AVTZ
HgO	2.03 [37]	2.07	QCISD(T)/60VDZ
$HgCl_2$	2.25–2.44 [34, 38, 39]	2.30	QCISD/60VDZ
		2.32	B3LYP/60VDZ
$HgBr_2$	2.378 [40]	2.40	CCSD(T)/AVTZ
		2.46	B3LYP (60MDF; 60VDZ)

a) All predictions from Wilcox *et al.* [12–14, 19] with the exception of SDD and CEP-121G basis sets, which were sourced from Krishnakumar and Helble [15].

provide accurate predictions. The QCISD(T)/60VDZ level of theory predicts a bond distance of 2.07 Å for HgO, which agrees reasonably well with the experimental value [37] of 2.03 Å from X-ray diffraction measurements. The HgBr bond distance was measured by Tellinghuisen and Ashmore [24] using emissions spectra photography, with an estimated bond distance of 2.62 Å, which matches exactly with the predicted value from B3LYP/60VDZ. Experimental results of Deyanov *et al.* [40] yield an Hg–Br bond distance within the $HgBr_2$ molecule of 2.378 Å. In general, the CCSD(T)/AVTZ level of theory predicts both the HgBr and $HgBr_2$ geometries reasonably accurately, deviating from experiment by 0.08 and 0.03 Å, respectively.

In addition to the spectroscopic and structure comparison, the enthalpy changes of the reactions of interest have also been predicted and directly compared to available experimental data. Table 24.3 shows both thermochemical and kinetic parameter predictions along with available experimental estimates for reaction enthalpies. In particular, Reaction 1 has received a lot of attention because of the discrepancies reported in the literature and it has been established as the rate-determining step for homogeneous Hg oxidation. The rate constant has been measured experimentally by Donohoue *et al.* [41] using laser-induced fluorescence and by Horne *et al.* [42] using flash photolysis. An effective second-order rate constant of $4.57 \times 10^{11}\ cm^3\ mol\ s^{-1}$ was calculated by Donohoue *et al.* from their reported Arrhenius expression at 260 K and 1 atm. Similarly, the second-order rate constant reported by Horne *et al.* at 393 K and 1 atm is $1.95 \times 10^{13}\ cm^3\ mol\ s^{-1}$. There has been one quantum-based theoretic prediction for the rate constant of the forward recombination pathway of Reaction 1 by

Table 24.3 Comparison between thermochemical (reaction enthalpy) and kinetic (rate constant) parameters of mercury oxidation via chlorine-containing compounds over various levels of theory.

Reaction	*Thermochemistry*		*Kinetics*		Level of theory
	ΔH_{rxn} (kcal mol^{-1}) Experiment [38]	Prediction	A (cm^3 mol s^{-1}) Prediction	E_a (kcal mol^{-1})	
R1. $Hg + Cl \leftrightarrow HgCl$	−24.91	−25.41	2.34[a)][11]	2.12	MP2/CEP-121G [15]
Reverse R1: $HgCl \leftrightarrow Hg + Cl$	24.91	25.27	2.42[b)][8]	15.7	QCISD/60VDZ [14]
R2. $Hg + O \leftrightarrow HgO$	−4.00[43]; −8.92[44]; −13.97[39]; −64.22	−10.58	5.62[c)][5]	3.03	QCISD(T)/60VDZ [13]
R3. $Hg + Cl_2 \leftrightarrow HgCl + Cl$	33.07	31.79	6.15 [13]	43.3	B3LYP/60VDZ [12]
		33.00	4.52 [13]	35.9	QCISD/CEP-121G [15]
R4. $Hg + Cl_2 \leftrightarrow HgCl_2$	−51.63	−55.03	1.77 [5]	8.64	B3LYP/60MDF [13]
R5. $Hg + HCl \leftrightarrow HgCl + H$	78.24	79.00	1.93 [13]	93.3	B3LYP/60VDZ [12]
		79.99	2.76 [15]	79.7	QCISD(T)/SDD [15]
R6. $Hg + HOCl \leftrightarrow HgCl + OH$	31.21	29.65	3.06 [13]	36.6	B3LYP/60VDZ [12]
		30.69	2.69 [14]	31.8	QCISD(T)/SDD [15]
R7. $HgCl + Cl \leftrightarrow HgCl_2$	−82.70	−79.44	7.00[c)][11]	8.567	B3LYP/60MDF [13]
		−83.79	2.02[d)][10]	1.20	MP4/SDD [15]
R8. $HgCl + Cl_2 \leftrightarrow HgCl_2 + Cl$	−24.72	−24.32	1.43 [9] to 2.47 [10]	0	B3LYP/60MDF
		−24.33	5.18[e)][4]	−3.40	B3LYP/MDF60 [15]
R9. $HgCl + HCl \leftrightarrow HgCl_2 + H$	20.46	20.50	1.95 [9]	24.9	QCISD/60MDF [14]
		20.50	2.49 [13]	24.9	B3LYP/MHF60 [15]
R10. $HgCl + HOCl \leftrightarrow HgCl_2 + OH$	−26.60	−26.47	1.74 [9] to 3.48 [10]	0.5	B3LYP/60MDF
		−26.45	3.28[e)][5]	0.3	B3LYP/MDF60 [15]

a) Temperature-dependent rate expression is $k = AT e^{-E_a/RT}$.
b) Units of A are in per second.
c) Temperature-dependent rate expression is $k = A\left(\frac{T}{298}\right)^{-n}$, with n listed in the E_a column.
d) Temperature-dependent rate expression is $k = AT e^{-E_a/RT}$.
e) Temperature-dependent rate expression is $k = AT^{2.4} e^{-E_a/RT}$.
Numbers in parentheses represent powers of 10.

Krishnakumar and Helble [15] at the MP2/CEP-121G level of theory, which is 3.77×10^9 and 1.52×10^{10} $cm^3\,mol\,s^{-1}$ at 260 and 939 K, respectively. The reverse rate constant of Reaction 1 may be estimated on the basis of available experimental equilibrium constant as the equilibrium constant is equal to the ratio of the forward and reverse rate constants. The reverse unimolecular decomposition of HgCl was investigated by Wilcox *et al*. [14] at the QCISD/60DVZ level of theory with a prediction of $1.45 \times 10^4\ s^{-1}$, compared to the experimentally calculated estimate of $4.31 \times 10^3\ s^{-1}$, derived from the measurement of Horne *et al*. at 393 K and 1 atm. Both MP2/CEP-121G and QCISD/60VDZ levels of theory predict the heat of reaction for HgCl decomposition accurately to within 1 kcal mol^{-1}, as shown in Table 24.3.

For the HgO formation reaction (R2), both the forward and reverse rate constants have been predicted by Wilcox [13] at 1 atm and over a temperature range of 298–2000 K, with the kinetic parameters of the forward recombination reaction presented in Table 24.3. It is noted that the thermal decomposition temperature of mercuric oxide is 773 K. There are no experimental rate constant data to compare to, but the heat of reaction has been compared against previously reported theoretical and experimental estimates. Estimating the enthalpy of formation of HgO has received a great deal of attention in the literature, and this formation enthalpy is required for accurate estimation of the reaction enthalpy. Theoretical calculations [39, 43, 44] have reported enthalpies of formation ranging between 60.2 and 81.2 kcal mol^{-1}, with an experimental estimate [38] of 10 kcal mol^{-1}. The reaction enthalpy estimates are listed in Table 24.3 and range from −4.00 to −13.97 kcal mol^{-1} based on theory to −64.22 kcal mol^{-1} based on experiment. The QCISD(T)/60VDZ level of theory predicts an enthalpy of reaction of −10.58, which agrees well with previous estimates and was used to determine the temperature-dependent rate constant parameters at 1 atm. Both thermochemical and kinetic parameters are available in Table 24.3 for Reactions 3–10, with the details of comparison and calculation available in the original work of these previous studies. The goal of these fundamental gas-phase submodels is to provide kinetic data to global reaction models that would otherwise be deficient owing to the limited experimental data available over the flue-gas temperature range of interest.

Bench-scale simulated flue-gas experiments have been carried out by Fry *et al*. [45] and Cauch *et al*. [1] to accurately measure Hg oxidation as a function of quench rate. Fry *et al*. [45] carried out experiments to evaluate the effects of quench rate and quartz surface area on Hg oxidation and performed a detailed kinetic modeling analysis of homogeneous Hg oxidation reactions. In their system, Hg and Cl_2 are injected into a natural gas-fired premixed burner to produce a radical pool representative of real combustion systems and passed through a quenching section following the hot temperature region in the furnace as the quench rate of the flue gas can influence the extent of Hg oxidation. Two different temperature profiles were employed, producing quench rates of −210 and −440 $K\,s^{-1}$. The Hg concentration in the reactor was 25 $\mu g\,m^{-3}$, while Cl_2 concentrations ranged from 100 to 600 ppmv (equivalent HCl concentration).

At Cl_2 concentrations of 200 ppmv, the larger quench rate resulted in a 52% increase in Hg oxidation compared to the lower quench rate. On the basis of kinetic modeling of the post-flame chlorine species, it was assumed that the Cl_2 molecules are converted to Cl radical species as they pass through the flame and then are subsequently converted predominantly to HCl. When investigating the effect of surface area of the quartz reactor, a threefold increase in surface area resulted in a 19% decrease in Hg oxidation, which is explained by the chlorine radical termination at the surface. It was concluded that quartz surfaces do not catalyze Hg oxidation reactions, but inhibit them, and that these surface interactions are negligible.

Recent experimental results of Cauch *et al.* [1] have shown that previously reported homogeneous Hg oxidation in the presence of chlorine may be exaggerated because of bias when using wet-chemistry measurement techniques. Linak *et al.* [46] have shown that Cl_2, in a simulated flue gas in the absence of SO_2, creates a bias in the Ontario Hydro method and overpredicts the concentrations of oxidized Hg. It has been shown that as little as 1 ppmv Cl_2 is enough to create a bias of 10–20% in the amount of oxidized Hg captured in the KCl solution. Within this study, the bias was eliminated by adding SO_2 to the flue gas or adding sodium thiosulfate ($Na_2S_2O_3$) to the KCl impinger. Similarly, Ryan and Keeney [47], in an actual flue-gas environment, have demonstrated that 10 ppmv Cl_2 added to the flue gas without SO_2 results in 91.5% oxidized Hg, with a decrease to 39% when the KCl impingers are spiked with sodium thiosulfate. A simulation study has been carried out by Gharebaghi *et al.* [4, 5] using the results from the experiments of Cauch *et al.* [1] with the corrected conditioning system to test the performance of the fundamental homogeneous Hg oxidation kinetics. Simulation of Hg speciation was carried out using the PREMIX module of the CHEMKIN II software package [48]. The Arrhenius parameters for the model predictions were taken from a combination of sources, with Reactions 1, 3, 5–10 included in the model in particular. The experimental rate constant determined by Donohoue *et al.* [41] was used for Reaction 1, model predictions from Niksa *et al.* [49] were used for Reactions 3 and 7, and quantum-level theoretical predictions were provided from Wilcox *et al.* [12, 14] for Reactions 5, 6, 8–10. Additional supporting mechanisms include chlorine chemistry from Roesler *et al.* [50], C/H/O mechanism by Dreyer *et al.* [51], and the Leeds SO_x and NO_x mechanism [52], resulting in a global combustion model of 80 species and 361 reactions. Figure 24.1 shows the results of the simulation predictions and their comparison to the bench-scale experiments of Cauch *et al.* [1] The model provides reasonable agreement with the experimental data at the 440 K s^{-1} quench rate, but underpredicts the data at 210 K s^{-1}.

The experimentally derived activation energies and rate constants can have significant errors due to wall effects as well as uncertainties in the determination of mercury and its compounds down to parts per billion and lower levels in flue gas. Noting these potentially large experimental uncertainties introduced by heterogeneous chemistry occurring on the reactor walls, and the measurement uncertainties, the models appear to reasonably reflect the experimental data.

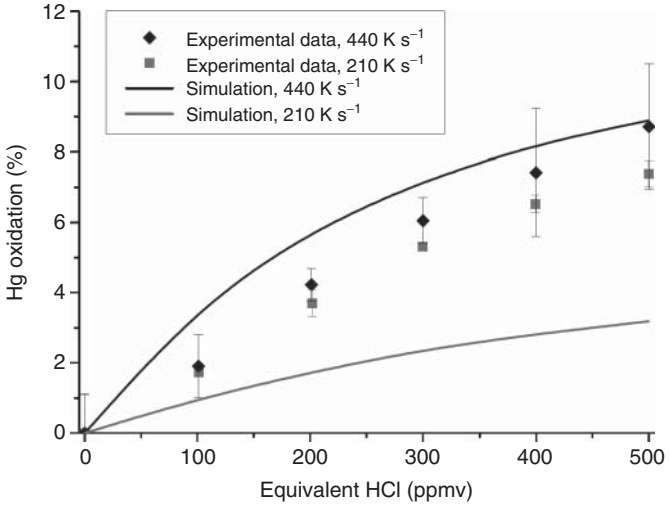

Figure 24.1 Error bars represent the standard deviation from analysis of multiple experiments.

24.2.2 Mercury–Bromine Chemistry

Significant attention has been paid to Hg oxidation via bromine, in addition to chlorine, because of the enhanced Hg oxidation kinetics of Br-containing compounds. Previous investigations report that bromine reacts faster than chlorine toward the production of $HgBr_2$. Similar to the Hg oxidation reactions involving Cl-containing species, Gharebaghi *et al.* [4] have also simulated Hg oxidation based on the following reactions:

$$Hg + Br \leftrightarrow HgBr \quad \text{(R11)}$$

$$Hg + Br_2 \leftrightarrow HgBr + Br \quad \text{(R12)}$$

$$Hg + HBr \leftrightarrow HgBr + H \quad \text{(R13)}$$

$$Hg + HOBr \leftrightarrow HgBr + OH \quad \text{(R14)}$$

$$HgBr + Br \leftrightarrow HgBr_2 \quad \text{(R15)}$$

$$HgBr + Br_2 \leftrightarrow HgBr_2 + Br \quad \text{(R16)}$$

$$HgBr + HBr \leftrightarrow HgBr_2 + H \quad \text{(R17)}$$

$$HgBr + HOBr \leftrightarrow HgBr_2 + OH \quad \text{(R18)}$$

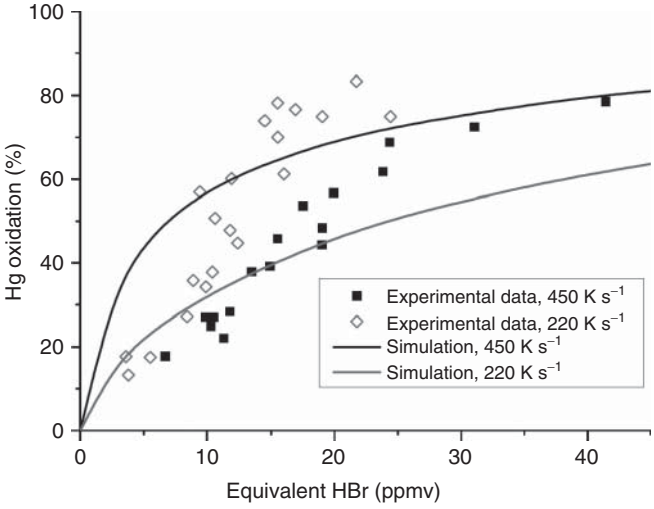

Figure 24.2 Comparison of measured and predicted Hg oxidation with HBr addition at two different reactor temperature quench rates [4].

Similar to the methodology previously discussed, Gharebaghi *et al*. [4] have used a variety of fundamentally derived rate parameters to simulate the global oxidation behavior of these reactions and have directly compared to experimental predictions of Cauch *et al*. [1], as shown in Figure 24.2. The rate parameters of Reaction 11 were taken from the experiments of Donohoue *et al*. [53] using laser-induced fluorescence, while the rate parameters of Reactions 14, 16, and 18 were taken from work carried out by Niksa *et al*. [54] The rate parameters for Reaction 15 was calculated from first principles by Goodsite *et al*. [55], while the parameters for Reactions 12, 13, and 17 were provided by Wilcox and Okano [19] and are based on first-principle quantum mechanical calculations. Table 24.4 provides a fairly complete list of thermochemical and kinetic parameters associated with 8 of the 10 Hg–Br reactions of interest. In previous work, Wilcox and Okano [19] compared their predicted rate data of Reactions 11, 12, and 15 to available experimental [53, 56] and theoretical [55–60] data in the literature. In particular, the theoretical rate constant prediction of 3.84×10^{11} cm^3 mol s^{-1} at the CCSD(T)/AVTZ level of theory for the forward direction of Reaction 11 agrees well with other theoretical [56–59] (ranging between 1.80×10^{11} and 1.92×10^{12} cm^3 mol s^{-1}) and experimental [53] (ranging between 1.08×10^{11} and 3.25×10^{11} cm^3 mol s^{-1}) estimates at 298 K and 1 atm. In addition, for Reaction 12, the theoretical rate constant prediction of 9.9×10^{-8} cm^3 mol s^{-1} at the B3LYP/60VDZ level of theory for the forward direction agrees well with a slight underprediction compared to other theoretical calculations [60], which range between 1.96×10^{-7} and 3.25×10^{-7} cm^3 mol s^{-1} at 298 K and 1 atm. Additional details are available in the manuscript of Wilcox and Okano [19].

Table 24.4 Comparison between thermochemical (reaction enthalpy) and kinetic (rate constant) parameters of mercury oxidation via bromine-containing compounds over various levels of theory.

Reaction	*Thermochemistry*		*Kinetics*		Level of theory [19]
	ΔH_{rxn} (kcal mol^{-1})		A (cm^3 mol s^{-1})	E_a (kcal mol^{-1})	
	Experiment [38]	Prediction	Prediction		
R11. Hg + Br ↔ HgBr	−16.51	−16.72	2.00[a)][12]	1.91	B3LYP/60VDZ
		−15.74	4.00[a)][11]	0.85	CCSD(T)/AVTZ
R12. Hg + Br_2 ↔ HgBr + Br	29.56	28.83	9.76 [14]	26.49	B3LYP/60VDZ
		31.59	1.15 [15]	30.08	CCSD(T)/AVTZ
R13. Hg + HBr ↔ HgBr + H	70.95	67.69	1.86 [13]	71.58	B3LYP/60VDZ
R15. HgBr + Br ↔ $HgBr_2$	−72.02	−71.94	2.00[a)][12]	9.18	CCSD(T)/AVTZ
		−70.13	8.00[a)][10]	7.644	B3LYP/60MDF
R16. HgBr + Br_2 ↔ $HgBr_2$ + Br	−25.95	−24.61	4.02 [11]	0.87	CCSD(T)/AVTZ
R17. HgBr + HBr ↔ $HgBr_2$ + H	15.44	14.28	9.41 [12]	18.68	B3LYP/60MDF

a) Temperature-dependent rate expression is $k = A\left(\frac{T}{298}\right)^{-n}$ with n listed in the E_a column.
Numbers in parentheses represent powers of 10.

The concentration of equivalent HBr was varied between 0 and 45 ppmv compared to a range of 0–500 ppmv of equivalent HCl as HBr dissociates more readily than HCl, resulting in a greater quantity of Br radicals for Hg oxidation. The homogeneous Hg oxidation model via bromine predicts that oxidation begins at a higher temperature than in the case of chlorine, at approximately 1100 K compared to 800 K (chlorine). The simulated results are in reasonable agreement with experiment for the 450 K s^{-1} quench rate above 25 ppmv equivalent HBr, but overestimate oxidation at lower concentrations. On the other hand, for the 220 K s^{-1} quench rate, the simulations underpredict oxidation at high temperature and show reasonable agreement at concentrations less than 10 ppmv equivalent HBr. Owing to the disagreement between the simulation predictions and experiments, it is clear that additional work is still required in this area. It is also noted that there is substantial uncertainty in the experimentally derived kinetic parameters.

From these previous combined modeling-experimental studies it is clear that homogeneous Hg oxidation is only one aspect of the complete mechanism in the complex flue-gas environment. In reality, surfaces are present in the form of unburned carbon, which may serve to both adsorb and oxidize Hg. Oxidized Hg may be captured in existing downstream wet FGD units and Hg^p may be captured via ESPs or FFs. Therefore, understanding the mechanism of Hg reactivity across carbon surfaces is imperative to its effective control.

24.3
Heterogeneous Chemistry

24.3.1
Mercury Adsorption on Activated Carbon

AC has been extensively tested in laboratory- and full-scale systems and has shown the capacity to capture both elemental and oxidized Hg in coal combustion flue gas. A relatively large amount of AC injection is required for the control of Hg from subbituminous-coal- or lignite-combustion flue gas. Depending on the system conditions, an AC-to-mercury mass ratio of at least 3000–20 000 (C/Hg) may be necessary to achieve 90% Hg removal [61–63]. Currently, the design of more effective Hg capture technology is limited by incomplete understanding of the mechanism(s) of Hg oxidation and adsorption on carbon surfaces [64].

The development of accurate fundamental models for Hg–AC reactivity requires careful characterization experiments on materials exposed to well-controlled reaction conditions. Therefore, an overview of such experiments will be discussed before the theoretical model efforts. It is generally accepted that acidic sites on the surface are responsible for elemental Hg capture on AC [65, 66]. In its atomic state, Hg acts as a base in that it has the propensity to oxidize (i.e., donates electrons to a surface or another gas-phase molecule); therefore, Hg will readily interact with acidic sites on the carbon surface. However, once oxidized, and thus acidic in nature, Hg species are thought to compete with acidic gases for the basic sites available on the carbon surface.

The presence of halogens (i.e., bromine, chlorine, and iodine) promotes Hg oxidation on carbon surfaces [66, 67]. Subsequently, AC demonstrates higher Hg removal performance in the flue gas of coals with greater chlorine content, as the combustion of such coal results in a higher concentration of HCl in the flue gas. Hutson *et al*. [68] exposed brominated and chlorinated AC to Hg-laden simulated flue gas and characterized the sorbents using X-ray absorption spectroscopy (XAS) and X-ray photoelectron spectroscopy (XPS). Within this work no evidence was found for homogeneous oxidation of Hg, and no Hg was found present on the AC surface; however, oxidized Hg was found on the surface, present as a chlorinated or brominated species. It is important to note that owing to the low coverage of Hg on the carbon, the speciation of Hg was not determined. Given the results, the authors proposed Hg capture on chlorinated and brominated carbons occurs via surface oxidation of Hg with subsequent adsorption on the carbon surface. Similar to its role in homogeneous Hg oxidation, bromine is thought to have a stronger promotional effect on Hg oxidation/adsorption, but the reason for the difference between bromine and chlorine is not well understood. Recently, the Hg oxidation was demonstrated on a wood-derived Cl-promoted AC in both N_2 and flue gas [69]. The adsorption of Hg on AC was shown to be a chemisorption process, where all Hg was oxidized to Hg^{2+} on the surface as a result of chlorine promotion. While chlorine was consumed, Hg^{2+} was still noted as being present in the outlet gas, indicating that the AC was also capable of catalyzing Hg oxidation.

Huggins *et al*. [70] characterized AC samples after testing in Hg-laden simulated flue-gas conditions using X-ray absorption fine structure (XAFS) spectroscopy. The XAFS results revealed that chlorine and sulfur are adsorbed on the AC surface after exposure to HCl and SO_2, and Hg-anion chemical bonds are formed in the sorbent materials. They suggest that the acidic flue-gas species (e.g., HCl, HNO_3, H_2SO_4) promote the creation of active sites for Hg chemisorption on the carbon surface, and that an oxidation process, either in the gas phase or simultaneously as the Hg atom interacts with the sorbents, is involved in the capture of Hg. Olson *et al*. [66] performed fixed-bed tests with various gas conditions for Hg and $HgCl_2$ adsorption on AC and found that the presence of both HCl and NO_2 reduced the induction period of Hg oxidation, and that in general acid flue-gas components significantly impacted the adsorption of oxidized Hg species. The formation and presence of the oxidized form, $Hg(NO_3)_2$, was observed in the effluent gas in the presence of NO_2, but in the absence of HCl. Laumb *et al*. [71] carried out surface analyses using XPS on ACs exposed to Hg-laden simulated flue gas (e.g., SO_2, NO_2, HCl, H_2O), but were unable to determine the oxidative state of surface-bound Hg due to interference with silicon (Si), which is present at comparable levels to Hg within the carbon matrix. Wilcox *et al*. [72] investigated the binding mechanism of Hg on brominated AC sorbents with a combination of XPS and theoretical modeling. It was found that Hg exists in the oxidized forms on brominated carbon surfaces, as shown in Figure 24.3.

Ab initio electronic structure investigations based on density functional theory (DFT) have been conducted to elucidate the interaction of Hg with AC, using simplified carbon models to represent AC. There have been a limited number of theoretical investigations, and, to the authors' knowledge, the effect of acid flue-gas species on Hg-AC interactions has not been investigated. AC is very difficult to model given its highly inhomogeneous structure. Several initial theoretical investigations have been conducted using cluster models to represent graphene, ranging from single benzene rings [73] to multiple fused rings [74] with embedded halogens as shown in Figure 24.4.

Carbon with Cl-containing functional groups exhibits enhanced Hg adsorption capacity. Furthermore, the most stable Hg surface species was HgCl, while Hg and $HgCl_2$ were found to be thermodynamically unstable on these simplified surfaces of AC [74]. Theoretical calculations by Olson *et al*. [76] supported the role of acidic sites on the AC in Hg capture. They hypothesized that HCl is energetically stable at the cationic zigzag edge sites of AC and proposed three possible models of Hg oxidation:

1) Hg charge transfer complex forms on the cationic center of HCl on AC and is subsequently attacked by Cl^-,
2) elemental Hg interacts simultaneously with the cationic HCl-AC site and Cl^-, or
3) oxidation by the dictation site formed by HCl and NO_2 on AC.

Olsen *et al*. [76] suggested that Hg has the propensity to be oxidized by donating its electrons to a surface or another gas-phase molecule; therefore, in its elemental

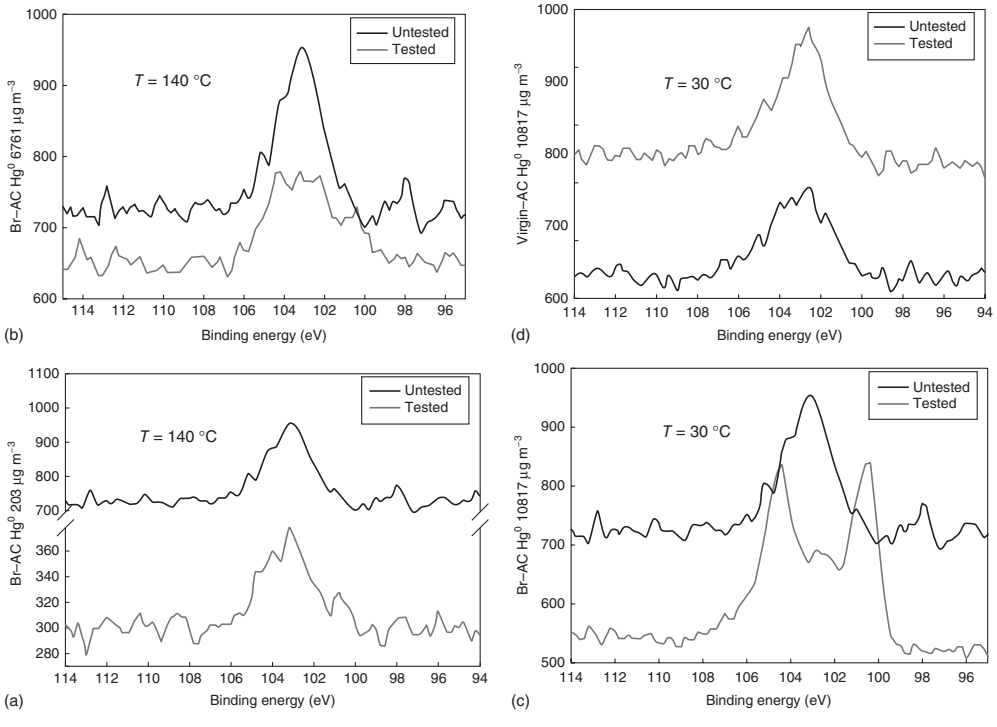

Figure 24.3 Hg 4f core level XPS spectra for activated carbon sorbents at various indicated conditions; (a–c) brominated AC sorbents and (d) virgin AC sorbent [72]. (Reprinted with permission from (Wilcox et al., J Air & Waste Manag. Assoc., 61(4), 418, 2011). Copyright (2011) Taylor & Francis.)

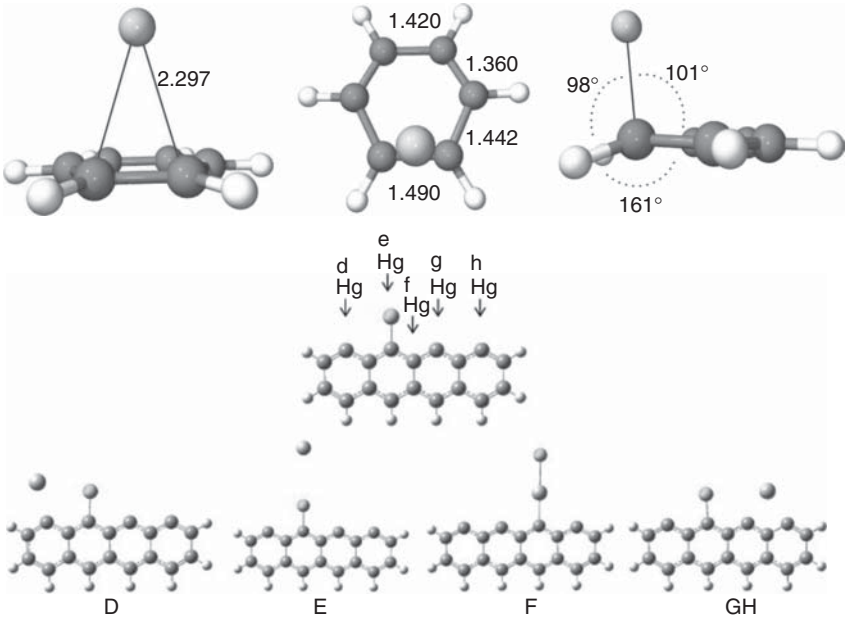

Figure 24.4 Hg–benzene complex investigated at the MP2/AVDZ level of theory (top) [73] (reprinted with permission from (Steckel, Chem. Phys. Lett., 409, 322, 2005). Copyright (2005) Elsevier.) and Hg-halogenated fused rings calculated at the B3LYP/LANL2DZ level of theory (bottom) [75]. (reprinted with permission from (Padak et al., Carbon, 47(12), 2855, 2009). Copyright (2009) Elsevier.)

state, Hg acts as a Lewis base with the desire to interact with an acidic site, thereby forming a strong C–Hg covalent bond on the carbon surface.

More recent investigations have used plane-wave DFT to model AC, which allows for the use of periodic systems such as a graphene. Graphene ribbons with exposed edge sites have been used for investigations of the reactivity of carbonaceous surfaces to various gas species [77]. Several investigations support the zigzag carbene structure model, where the zigzag edge site acts as a Lewis base and reacts with acid gas components thereby serving as a potential adsorption site for oxidized Hg [77, 78]. A recent DFT study [79] on the effect of chemical functional groups on Hg adsorption on carbon surfaces supports this suggestion. The study indicates that an embedded halogen atom promotes chemisorption on the neighboring site, which is consistent with experimental results, and indicative of Hg oxidation. Results also indicate a varying effect of organic groups on Hg adsorption, with lactone, carbonyl, and semiquinone groups promoting Hg chemisorption while phenol and carboxyl functional groups promote physisorption and reduce overall Hg capture. A mechanistic study of Hg oxidation due to halides on carbon materials proposes that the interactions of microcrystalline graphitic structures with halide ions result in the withdrawal of electrons from the graphitic structure, producing a strong Lewis

acid site [80], with Hg adsorption combined with the electron-transfer results in Hg oxidation.

To date, little work has been conducted on the effect of Br on Hg-AC interactions. Wilcox *et al*. [72] investigated the binding mechanism of Hg on brominated AC sorbents with a combination of experimental work, as discussed previously, and quantum-mechanical modeling using a nine-benzene-rings-wide graphene ribbon. Consistent with Padak and Wilcox's [75] results for Hg adsorption in the presence of chlorine, it was found that HgBr species are more stable on the carbon surface than $HgBr_2$ species. Furthermore, DFT and density of states (DOSs) calculations indicate that Hg is more stable when it is bound to the edge C atom interacting with a single Br atom bound atop of Hg. However, while the form of Hg adsorbed on the AC surface may be oxidized, the exact speciation of the adsorbed Hg is remains in question. Furthermore, the Hg adsorption mechanism on the carbon surface and the effects of the flue-gas components are not well understood. Additional work, including closely coupled experimental and theoretical investigations, is required to determine the binding mechanism of Hg on AC sorbents in various flue-gas environments and to further elucidate the adsorption mechanism of Hg on AC.

24.3.2 Mercury Adsorption on Precious Metals

In general, precious metal adsorption of Hg has been applied to Hg capture from fuel gases of coal gasification processes as these metals, in contrast to carbon-based sorbents, may withstand the high temperatures of gasification processes. For gasification applications, the product is termed a *fuel gas*, and consists primarily of H_2, CO_2, and CO, while in the case of traditional coal combustion, the exhaust gas is termed a *flue gas* and is comprised primarily of N_2 and CO_2.

Precious metals, including palladium (Pd), platinum (Pt), gold (Au), iridium (Ir), and rhodium (Rh), have traditionally been used as modifiers for graphite-tube atomic absorption or emission analysis of solid and liquid samples. Among them, Pd has been identified as the best modifier for the adsorption of Hg [16]. In a study carried out by Steckel [81], DFT is used to carry out electronic structure calculations on slab models representing the (001) and (111) surfaces of silver (Ag), Au, copper (Cu), nickel (Ni), Pd, and Pt. Relatively strong binding for all of the metals was noted, with binding energies of ~1 eV for Pt and Pd. However, the DFT method used appears to underestimate the adsorption energy when compared directly to experimental results. Mercury has been predicted to have a stronger bond with the (001) surface, where fourfold hollow sites exist, in contrast to the threefold hollow sites on (111) surfaces. Aboud *et al*. [82] performed a DFT study of Pd alloyed with small amounts Au, Ag, and Cu and found that doping of the Pd surface increased the overall binding energy of Hg, which is beneficial for a sorption process. Furthermore, the binding energy increased the most when the dopants remained subsurface. In a continuation of the work, Sasmaz *et al*. [83] showed that Pd is primarily responsible for interacting with Hg in both alloys and

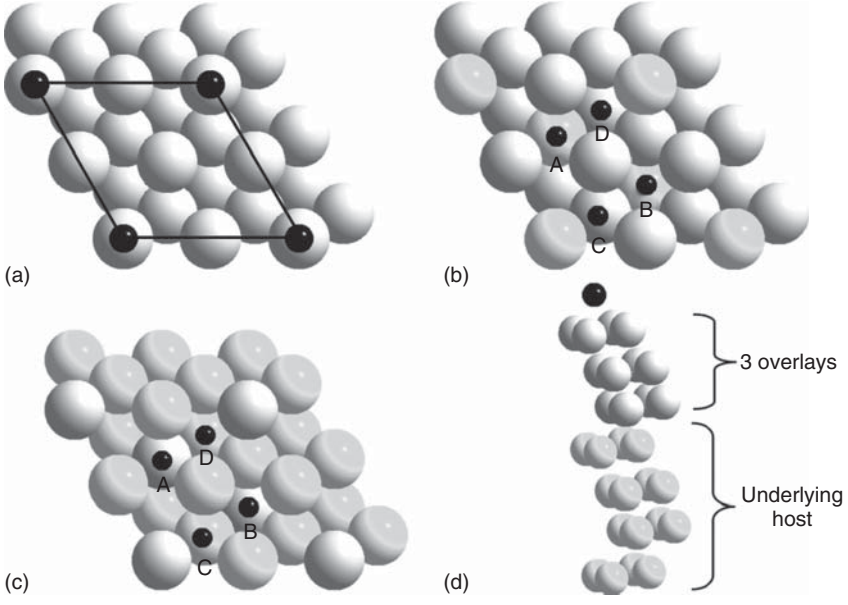

Figure 24.5 (a) Scheme of a supercell of (111) surfaces. (b) Threefold adsorption sites of Pd_3M binary alloys: (A) pure-hexagonal close packed (hcp) site, (B) pure-face-centered cubic (fcc) site, (C) mixed-hcp site, and (D) mixed-fcc site. (c) Threefold adsorption sites of PdM_3 binary alloys: (A) pure-hcp site, (B) pure-fcc site, (C) mixed-hcp site, and (D) mixed-fcc site. (d) Side view of 3Pd/M(111) structure [83]. (Reprinted with permission from (Sasmaz, et al., J. Phys. Chem. C, 113, 7813, 2009). Copyright (2009) American Chemical Society.)

overlays and that the interaction is a result of overlap between the s- and p-states of Pd and the d-state of Hg. Figure 24.5 shows various adsorption sites of Hg on binary alloys and overlays of Pd with other metals, M, such that M represents either gold, silver, or copper.

Jain *et al*. [84] theoretically screened potential high-temperature metal sorbents for Hg capture in syngas streams. Using DFT predictions, the enthalpy of amalgamation and oxidation for metals was evaluated to predict the capability of Hg sorption and oxidation in the gas stream, demonstrating that Pd has the highest amalgamation enthalpy of all metals. Figure 24.6 shows the Hg amalgam formation enthalpy versus the binary oxide formation enthalpy to clarify the tendency of various metals for amalgamation and oxidation. Metals above the O_2 gas chemical potential line (i.e., dashed horizontal line) are estimated to form oxides and metals to the right of the Hg gas chemical potential (i.e., dashed vertical line) are estimated to form amalgams in the syngas stream. Metals satisfying both criteria (i.e., Section (II) in Figure 24.6) were found to form oxides rather than amalgams according to the grand canonical potential predictions. An ideal metal, which amalgamates without oxidizing, is located in Section (IV) of Figure 24.6. No metals are available in the most desirable area, but Pd is the closest to the area, indicating that Pd is the most promising metal for Hg capture.

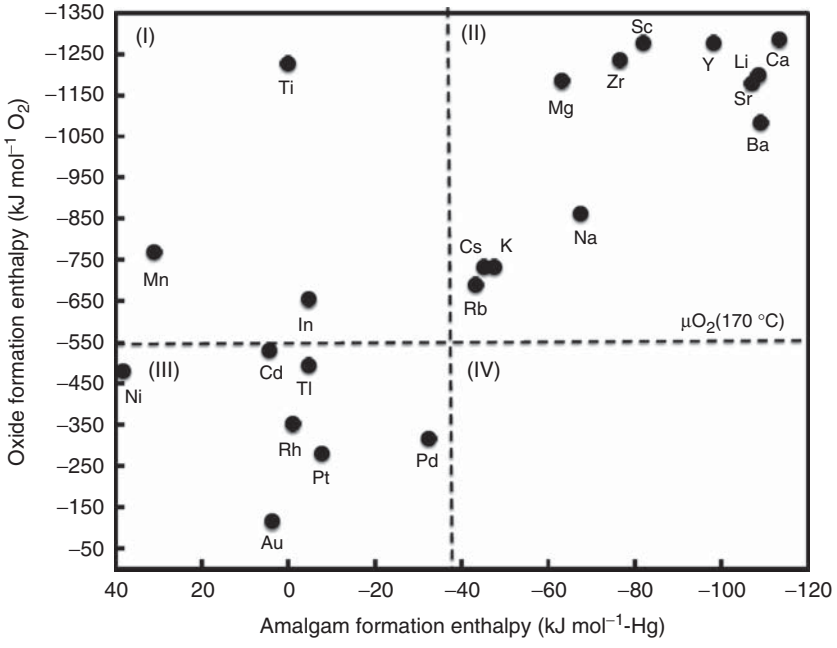

Figure 24.6 Estimated amalgam formation enthalpies of binary Hg amalgam versus binary oxide, normalized per mol of Hg and per mol of O_2, respectively. Dashed horizontal and vertical lines represent the O_2 gas and Hg gas chemical potentials, respectively [84]. (Reprinted with permission from (Jain et al., Chem. Eng. Sci., 65, 3025,2010). Copyright (2010) Elsevier.)

Earlier experiments have validated the mechanisms of reactivity proposed by theory. For example, Baltrus *et al*. [85, 86] showed some evidence of Hg amalgamation on Pd/Al_2O_3. Maximum Hg adsorption on Pd/Al_2O_3 occurs at 204 °C and at low loadings of Pd (<8.5 wt% Pd). An interesting finding is that Hg adsorption is suppressed by an excess of As; however, H_2S in fuel gas can improve this imbalance by moderately inhibiting the As adsorption while enhancing the Hg adsorption [86]. Poulston *et al*. [87] compared the Hg removal capacities of Pd and Pt sorbents supported on alumina and found that Pd is superior to Pt sorbents for Hg removal. This trend is supported by Figure 24.5, which indicates that Pt is located farther from the Section (IV) than Pd. The Hg removal capacity of both Pd and Pt sorbents increase with metal loading but decreases with sorbent temperature. Although most metal sorbent candidates exhibit poor capacities for Hg at temperatures greater than 204 °C, Pd proves to be an attractive sorbent for the Hg removal at elevated temperatures [16]. Fuel-gas substances that may affect the Hg adsorption on metal sorbents may include moisture, H_2S, CO, and H_2 [16]. Baldeck *et al*. [88] presented data on the use of Au traps for the quantitative fuel-gas separation of Hg in the form of an amalgam of Au_2Hg_3. It was suggested that Hg removal on Au is not affected by corrosive substances such as SO_2, H_2S, and organic compounds that may be present in flue gas.

24.4
Conclusions and Future Work

Atomistic modeling efforts have resulted in important insight into the homogeneous and heterogeneous mercury chemistry in power plant flue gases. Future work may focus upon the heterogeneous chemistry of mercury on common fly ash metal oxides, the ductwork walls within the power plants, and the SCR catalysts employed for reduction of NO*x*. Recent and past works [62, 89, 90] hint at a possible important role for iodine and its compounds for promoting the oxidation of mercury in flue gas. It is suggested that further work is merited on the halogens, including both the heterogeneous chemistry on carbon, as well as the gas phase chemistry involving chlorine, bromine, and iodine species.

References

1. Cauch, B., Silcox, G.D., Lighty, J.A.S., Wendt, J.O.L., Fry, A., and Senior, C.L. (2008) Confounding effects of aqueous-phase impinger chemistry on apparent oxidation of mercury in flue gases. *Environ. Sci. Technol.*, **42** (7), 2594–2599.
2. Wilcox, J. (2004) On the path to elucidating the speciation of mercury in the flue gases of coal combustion. PhD Thesis, The University of Arizona.
3. Padak, B. (2011) Mercury reaction chemistry in combustion flue gases from experiments and theory. PhD Thesis, Stanford University, Stanford, CA.
4. Gharebaghi, M., Gibson, J., Hughes, K.J., Irons, R., Porter, R.T.J., Pourkashanian, M., and Williams, A. (2010) A modeling study of mercury transformation in coal-fired power plants. Proceedings of the American Flame Research Committee 2010 Pacific Rim Combustion Symposium, Maui, HI, 2010.
5. Gharebaghi, M., Hughes, K., Porter, R., Pourkashanian, M., and Williams, A. (2011) Mercury speciation in air-coal and oxy-coal combustion: a modelling approach. *Proc. Combust. Inst.*, **33** (2), 1779–1786.
6. Wang, Y., Duan, Y., Yang, L., Zhao, C., and Xu, Y. (2010) Mercury speciation and emission from the coal-fired power plant filled with flue gas desulfurization equipment. *Can. J. Chem. Eng.*, **88** (5), 867–873.
7. Senior, C.L., Sarofim, A.F., Zeng, T., Helble, J.J., and Mamani-Paco, R. (2000) Gas-phase transformations of mercury in coal-fired power plants. *Fuel Process. Technol.*, **63** (2-3), 197–213.
8. Sliger, R., Going, D.J., and Kramlich, J. C. (1998) Kinetic Investigation of the High-Temperature Oxidation of Mercury by Chlorine Species.
9. Sliger, R.N., Kramlich, J.C., and Marinov, N.M. (2000) Towards the development of a chemical kinetic model for the homogeneous oxidation of mercury by chlorine species. *Fuel Process. Technol.*, **65**, 423–438.
10. Hall, B., Schager, P., and Lindqvist, O. (1991) Chemical reactions of mercury in combustion flue gases. *Water Air Soil Pollut.*, **56** (1), 3–14.
11. Widmer, N., Cole, J., Seeker, W.R., and Gaspar, J. (1998) Practical limitation of mercury speciation in simulated municipal waste incinerator flue gas. *Combust. Sci. Technol.*, **134** (1-6), 315–326.
12. Wilcox, J. (2009) A kinetic investigation of high-temperature mercury oxidation by chlorine. *J. Phys. Chem. A*, **113** (24), 6633–6639.
13. Wilcox, J. (2011) A kinetic investigation of unimolecular reactions involving trace metals at post-combustion flue gas conditions. *Environ. Chem.*, **8** (2), 207–212.
14. Wilcox, J., Robles, J., Marsden, D.C.J., and Blowers, P. (2003) Theoretically predicted rate constants for mercury oxidation by hydrogen chloride in coal

combustion flue gases. *Environ. Sci. Technol.*, **37** (18), 4199–4204.
15. Krishnakumar, B. and Helble, J.J. (2012) Determination of transition state theory rate constants to describe mercury oxidation in combustion systems mediated by Cl, Cl_2, HCl and HOCl. *Fuel Process. Technol.*, **94** (1), 1–9.
16. Granite, E.J., Myers, C.R., King, W.P., Stanko, D.C., and Pennline, H.W. (2006) Sorbents for mercury capture from fuel gas with application to gasification systems. *Indust. Eng. Chem. Res.*, **45** (13), 4844–4848.
17. Stevens, W.J., Krauss, M., Basch, H., and Jasien, P.G. (1992) Relativistic compact effective potentials and efficient, shared-exponent basis sets for the third-, fourth-, and fifth-row atoms. *Can. J. Chem.*, **70** (2), 612–630.
18. Figgen, D., Rauhut, G., Dolg, M., and Stoll, H. (2005) Energy-consistent pseudopotentials for group 11 and 12 atoms: adjustment to multi-configuration Dirac-Hartree-Fock data. *Chem. Phys.*, **311** (1-2), 227–244.
19. Wilcox, J. and Okano, T. (2011) Ab initio-based mercury oxidation kinetics via bromine at postcombustion flue gas conditions. *Energy Fuel*, **25** (4), 1348–1356.
20. Peterson, K.A., Figgen, D., Goll, E., Stoll, H., and Dolg, M. (2003) Systematically convergent basis sets with relativistic pseudopotentials. II. Small-core pseudopotentials and correlation consistent basis sets for the post-d group 16,Äì18 elements. *J. Chem. Phys.*, **119**, 11113.
21. Peterson, K.A. and Puzzarini, C. (2005) Systematically convergent basis sets for transition metals. II. Pseudopotential-based correlation consistent basis sets for the group 11 (Cu, Ag, Au) and 12 (Zn, Cd, Hg) elements. *Theor. Chem. Acc.: Theory Comput. Model. (Theor. Chim. Acta)*, **114** (4), 283–296.
22. Chase, M.W. Jr., (1998) *NIST-JANAF Thermochemical Tables*, Journal of Physical and Chemical Reference Data (Monograph), 4th edn, vol. 9, American Chemical Society, Washington, DC; American Institute of Physics for the National Institute of Standards and Technology, Woodbury, NY.
23. Tellinghuisen, J., Tellinghuisen, P.C., Davies, S.A., Berwanger, P., and Viswanathan, K. (1982) B → X transitions in HgCl and HgI. *Appl. Phys. Lett.*, **41** (9), 789–791.
24. Tellinghuisen, J. and Ashmore, J.G. (1982) The B → X transition in 200Hg 79Br. *Appl. Phys. Lett.*, **40** (10), 867–869.
25. Aylett, B. (1973) *Group IIB*, vol. 3, Pergamon Press, Elmsford, NY, pp. 187–328.
26. Bell, S., McKenzie, R., and Coon, J. (1966) The spectrum of $HgCl_2$ in the vacuum ultraviolet. *J. Mol. Spectrosc.*, **20** (3), 217–225.
27. Malt'sev, A.A., Selivanov, G.K., Yampolsky, V.I., and Zavalishin, N.I. (1971) *Nat. Phys. Sci.*, **231**, 157.
28. Adams, D.M. and Hills, D.J. (1978) Single-crystal infrared study and assignment for mercury (II) chloride and bromide. *J. Chem. Soc., Dalton Trans.*, (7), 776–782.
29. Braune, H. and Engelbrecht, G. (1932) On the Raman-effect of some inorganic halogenides in the liquid and gaseous state. *Z. Phys. Chem. Abt. B*, **19**, 303.
30. Sponer, H. and Teller, E. (1941) Electronic spectra of polyatomic molecules. *Rev. Mod. Phys.*, **13** (2), 75.
31. Clark, R.J.H. and Rippon, D.M. (1973) Vapour phase Raman spectra of mercury (II) chloride, mercury (II) bromide and mercury (II) iodide. v1 ($\Sigma + g$) band contours and the mercury-halogen bond polarisability derivatives. *J. Chem. Soc., Faraday Trans. 2*, **69**, 1496–1501.
32. Beattie, I.R. and Horder, J.R. (1970) Gas-phase Raman spectra of some dihalides of zinc and mercury, of "$GaCl_2$" and of $GaCl_2Br$ and $GaBr_2Cl$. *J. Chem. Soc. A*, 2433–2435.
33. Klemperer, W. and Lindeman, L. (1956) Infrared spectrum of mercuric chloride and bromide. *J. Chem. Phys.*, **25**, 397.
34. Kaupp, M. and von Schnering, H.G. (1994) Origin of the unique stability of condensed-phase Hg_2^{2+}. An ab initio investigation of MI and MII species (M = Zn, Cd, Hg). *Inorg. Chem.*, **33** (18), 4179–4185.
35. Strömberg, D., Strömberg, A., and Wahlgren, U. (1991) Relativistic quantum calculations on some mercury sulfide

molecules. *Water Air Soil Pollut.*, **56** (1), 681–695.
36. Cundari, T.R. and Yoshikawa, A. (1998) Computational study of methane activation by mercury (II) complexes. *J. Comput. Chem.*, **19** (8), 902–911.
37. Šćavničar, S. (1955) The crystal structure of trimercuric oxychloride, $HgCl_2$. 2HgO. *Acta Crystallogr.*, **8** (7), 379–383.
38. Chase, M.W. Jr., Davies, C.A., Downey, J.R., Fruirip, D.J., McDonald, R.A., and Syverud, A.N. (1985) *JANAF Thermochemical Tables, Part 1 Al-Co*, Journal of Physical and Chemical Reference Data, vol. 14 (Suppl. 1), 3rd edn, American Institute of Physics, p. 1.
39. Strömberg, D., Gropen, O., and Wahlgren, U. (1989) Non-relativistic and relativistic calculations on some Zn, Cd and Hg complexes. *Chem. Phys.*, **133** (2), 207–219.
40. Deyanov, R., Petrov, K., Ugarov, V., Shchedrin, B., and Rambidi, N. (1985) Automatic background subtraction in gas electron diffraction: the covariance matrix in least-squares structure-parameter analysis. *J. Struct. Chem.*, **26** (5), 698–703.
41. Donohoue, D.L., Bauer, D., and Hynes, A.J. (2005) Temperature and pressure dependent rate coefficients for the reaction of Hg with Cl and the reaction of Cl with Cl: A pulsed laser photolysis-pulsed laser induced fluorescence study. *J. Phys. Chem. A*, **109** (34), 7732–7741.
42. Horne, D., Gosavi, R., and Strausz, O. (1968) Reactions of metal atoms. I. The combination of mercury and chlorine atoms and the dimerization of HgCl. *J. Chem. Phy.*, **48**, 4758.
43. Shepler, B.C. and Peterson, K.A. (2003) Mercury monoxide: a systematic investigation of its ground electronic state. *J. Phys. Chem. A*, **107** (11), 1783–1787.
44. Dewar, M.J.S. and Jie, C. (1989) AM1 calculations for compounds containing mercury. *Organometallics*, **8** (6), 1547–1549.
45. Fry, A., Cauch, B., Silcox, G.D., Lighty, J.A.S., and Senior, C.L. (2007) Experimental evaluation of the effects of quench rate and quartz surface area on homogeneous mercury oxidation. *Proc. Combust. Inst.*, **31** (2), 2855–2861.
46. Linak, W.P., Ryan, J.V., Ghorishi, B.S., and Wendt, J.O.L. (2001) Issues related to solution chemistry in mercury sampling impingers. *J. Air Waste Manage. Assoc.*, **51** (5), 688–698.
47. Ryan, J.V. and Keeney, R.M. (2004) Symposium on Air Quality Measurement Methods and Technology, Research Triangle Park, NC, 2004.
48. Kee, R.J., Rupley, F.M., and Miller, J.A. (1993) CHEMKIN-2: A Fortran Chemical Kinetics Package for the Analysis of Gas-Phase Chemical Kinetics. Sandia Laboratories Report: 589-8009B. Sandia Laboratory.
49. Niksa, S., Helble, J.J., and Fujiwara, N. (2001) Kinetic modeling of homogeneous mercury oxidation: the importance of NO and H_2O in predicting oxidation in coal-derived systems. *Environ. Sci. Technol.*, **35** (18), 3701–3706.
50. Roesler, J.F., Yetter, R.A., and Dryer, F.L. (1995) Kinetic interactions of CO, NOx, and HCI emissions in postcombustion gases. *Combust. Flame*, **100** (3), 495–504.
51. Li, J., Zhao, Z., Kazakov, A., Chaos, M., Dryer, F.L., and Scire, J.J. Jr., (2007) A comprehensive kinetic mechanism for CO, CH_2O, and CH_3OH combustion. *Int. J. Chem. Kinet.*, **39** (3), 109–136.
52. University of Leeds *http://www.chem.leeds.ac.uk/Combustion?Combustion.html* (accessed 19 March 2014).
53. Donohoue, D.L., Bauer, D., Cossairt, B., and Hynes, A.J. (2006) Temperature and pressure dependent rate coefficients for the reaction of Hg with Br and the reaction of Br with Br: a pulsed laser photolysis-pulsed laser induced fluorescence study. *J. Phys. Chem. A*, **110** (21), 6623–6632.
54. Niksa, S., Naik, C.V., Berry, M.S., and Monroe, L. (2009) Interpreting enhanced Hg oxidation with Br addition at Plant Miller. *Fuel Process. Technol.*, **90** (11), 1372–1377.
55. Goodsite, M.E., Plane, J., and Skov, H. (2004) A theoretical study of the oxidation of Hg0 to HgBr2 in the troposphere. *Environ. Sci. Technol.*, **38** (6), 1772–1776.
56. Ariya, P.A., Khalizov, A., and Gidas, A. (2002) Reactions of gaseous mercury

with atomic and molecular halogens: kinetics, product studies, and atmospheric implications. *J. Phys. Chem. A*, **106** (32), 7310–7320.

57. Shepler, B.C., Balabanov, N.B., and Peterson, K.A. (2007) Hg + Br → HgBr recombination and collision-induced dissociation dynamics. *J. Chem. Phys.*, **127**, 164304.
58. Khalizov, A.F., Viswanathan, B., Larregaray, P., and Ariya, P.A. (2003) A theoretical study on the reactions of Hg with halogens: Atmospheric implications. *J. Phys. Chem. A*, **107** (33), 6360–6365.
59. Spicer, C., Satola, J., Abbgy, A., Plastridge, R., and Cowen, K. (2002) Kinetics of Gas-Phase Elemental Mercury Reactions with Halogen Species, Ozone, and Nitrate Radical Under Atmospheric Conditions, Battelle Columbus. Final Report to Florida Department of Environmental Protection under Contract AQ174 2002. DEP.
60. Balabanov, N.B., Shepler, B.C., and Peterson, K.A. (2005) Accurate global potential energy surface and reaction dynamics for the ground state of HgBr2. *J. Phys. Chem. A*, **109** (39), 8765–8773.
61. Matsumura, Y. (1967) Adsorption of mercury vapor on the surface of activated carbons modified by oxidation or iodization. *Atmos. Environ.*, **8** (12), 1321–1327.
62. Granite, E.J., Pennline, H.W., and Hargis, R.A. (2000) Novel sorbents for mercury removal from flue gas. *Ind. Eng. Chem. Res.*, **39** (4), 1020–1029.
63. Krishnan, S., Gullett, B.K., and Jozewicz, W. (1994) Sorption of elemental mercury by activated carbons. *Environ. Sci. Technol.*, **28** (8), 1506–1512.
64. Hower, J.C., Senior, C.L., Suuberg, E.M., Hurt, R.H., Wilcox, J.L., and Olson, E.S. (2010) Mercury capture by native fly ash carbons in coal-fired power plants. *Prog. Energy Combust. Sci.*, **36** (4), 510–529.
65. Mibeck, B.A.F., Olson, E.S., and Miller, S.J. (2009) $HgCl_2$ sorption on lignite activated carbon: analysis of fixed-bed results. *Fuel Process. Technol.*, **90** (11), 1364–1371.
66. Olson, E., Mibeck, B., Benson, S., Laumb, J., Crocker, C., Dunham, G., Sharma, R., Miller, S., and Pavlish, J. (2004) The mechanistic model for flue gas-mercury interactions on activated carbons: the oxidation site. *Prepr. Pap. - Am. Chem. Soc., Div. Fuel Chem.*, **49** (1), 279.
67. Ghorishi, B. and Gullett, B.K. (1998) Sorption of mercury species by activated carbons and calcium-based sorbents: effect of temperature, mercury concentration and acid gases. *Waste Manag. Res.*, **16** (6), 582.
68. Hutson, N.D., Attwood, B.C., and Scheckel, K.G. (2007) XAS and XPS characterization of mercury binding on brominated activated carbon. *Environ. Sci. Technol.*, **41** (5), 1747–1752.
69. Hu, C., Zhou, J., Luo, Z., and Cen, K. (2010) Oxidative adsorption of elemental mercury by activated carbon in simulated coal-fired flue gas. *Energy Fuel*, **25** (1), 154–158.
70. Huggins, F.E., Yap, N., Huffman, G.P., and Senior, C.L. (2003) XAFS characterization of mercury captured from combustion gases on sorbents at low temperatures. *Fuel Process. Technol.*, **82** (2-3), 167–196.
71. Laumb, J.D., Benson, S.A., and Olson, E.A. (2004) X-ray photoelectron spectroscopy analysis of mercury sorbent surface chemistry. *Fuel Process. Technol.*, **85** (6-7), 577–585.
72. Wilcox, J., Sasmaz, E., Kirchofer, A., and Lee, S. (1995) Heterogeneous mercury reaction chemistry on activated carbon. *J. Air Waste Manage. Assoc.*, **61** (4), 418.
73. Steckel, J. (2005) Ab initio modelling of neutral and cationic Hg-benzene complexes. *Chem. Phys. Lett.*, **409** (4-6), 322–330.
74. Padak, B., Brunetti, M., Lewis, A., and Wilcox, J. (2006) Mercury binding on activated carbon. *Environ. Progr.*, **25** (4), 319–326.
75. Padak, B. and Wilcox, J. (2009) Understanding mercury binding on activated carbon. *Carbon*, **47** (12), 2855–2864.
76. Olson, E.S., Azenkeng, A., Laumb, J.D., Jensen, R.R., Benson, S.A., and Hoffmann, M.R. (2009) New developments in the theory and modeling of

mercury oxidation and binding on activated carbons in flue gas. *Fuel Proc. Technol.*, **90** (11), 1360–1363.

77. Radovic, L.R. and Bockrath, B. (2005) On the chemical nature of graphene edges: origin of stability and potential for magnetism in carbon materials. *J. Am. Chem. Soc.*, **127** (16), 5917–5927.
78. Huggins, F.E., Huffman, G.P., Dunham, G.E., and Senior, C.L. (1999) XAFS examination of mercury sorption on three activated carbons. *Energy Fuel*, **13** (1), 114–121.
79. Liu, J., Cheney, M.A., Wu, F., and Li, M. (2011) Effects of chemical functional groups on elemental mercury adsorption on carbonaceous surfaces. *J. Hazard. Mater.*, **186** (1), 108–113.
80. Qu, Z., Chang, J.J., Hsiung, T.L., Yan, N., Wang, H.P., Dod, R., Chang, S.G., and Miller, C. (2010) Halides on carbonaceous materials for enhanced capture of Hg^0: Mechanistic study. *Energy Fuel*, **24** (6), 3534–3539.
81. Steckel, J.A. (2008) Density functional theory study of mercury adsorption on metal surfaces. *Phys. Rev. B*, **77** (11), 115412.
82. Aboud, S., Sasmaz, E., and Wilcox, J. (2008) Mercury adsorption on PdAu, PdAg and PdCu alloys. *Main Group Chem.*, **7** (3), 205–215.
83. Sasmaz, E., Aboud, S., and Wilcox, J. (2009) Hg binding on Pd binary alloys and overlays. *J. Phys. Chem. C*, **113** (18), 7813–7820.
84. Jain, A., Seyed-Reihani, S.A., Fischer, C.C., Couling, D.J., Ceder, G., and Green, W.H. (2010) Ab initio screening of metal sorbents for elemental mercury capture in syngas streams. *Chem. Eng. Sci.*, **65** (10), 3025–3033.
85. Baltrus, J.P., Granite, E.J., Stanko, D.C., and Pennline, H.W. (2008) Surface characterization of Pd/Al_2O_3 sorbents for mercury capture from fuel gas. *Main Group Chem.*, **7** (3), 217–225.
86. Baltrus, J.P., Granite, E.J., Pennline, H.W., Stanko, D., Hamilton, H., Rowsell, L., Poulston, S., Smith, A., and Chu, W. (2010) Surface characterization of palladium-alumina sorbents for high-temperature capture of mercury and arsenic from fuel gas. *Fuel*, **89** (6), 1323–1325.
87. Poulston, S., Granite, E.J., Pennline, H.W., Myers, C.R., Stanko, D.P., Hamilton, H., Rowsell, L., Smith, A.W.J., Ilkenhans, T., and Chu, W. (2007) Metal sorbents for high temperature mercury capture from fuel gas. *Fuel*, **86** (14), 2201–2203.
88. Baldeck, C.M., Kalb, G.W., and Crist, H.L. (1974) Determination of elemental mercury in an emission source having a high sulfur dioxide concentration by amalgamation with gold and ultraviolet pectrophotometry. *Anal. Chem.*, **46** (11), 1500–1505.
89. Granite, E.J., Pennline, H.W., and Hargis, R.A. (1998) Sorbents for Mercury Removal from Flue Gas 1998, DOE Topical Report TR-98-01. DOE.
90. Durham, M.D., Sjostrom, S., and Baldrey, K.E. (2013) Method and system for controlling mercury emissions from coal-fired thermal processes. US Patent 8,496,894, Jul. 30, 2013.